Journal of the European Ceramic Society **18** (1998) 87–93

PII: S0955-2219(97)00088-5
0955-2219/98/$19.00 + 0.00

Influence of Sample Deformation and Porosity On Mechanical Properties by Instrumented Microindentation Technique

Kai Duan* and Rolf W. Steinbrech

Forschungszentrum Jülich GmbH, Institut für Werkstoffe der Energietechnik, D-52425 Jülich, Germany

(Received 4 October 1996; accepted 27 February 1997)

Abstract

General equations are derived for evaluating the contributions of the non-penetration displacements to the apparent Young's modulus and hardness measured in an instrumented microindentation test. An idealized disk model is proposed to simulate the roles of porosity and sample displacements in determining Young's modulus and hardness from the indentation curve. The model is then applied to experimental data obtained from the indentation tests completed with separated and bonded yttria-stabilized zirconia (YSZ) thermal barrier coating layers. It is shown that in an instrumented microindentation test of a thin material plate, large scatter in the mechanical properties may originate from non-penetration displacements which usually increase with decreasing sample thickness. Predictions are also made for the apparent E-H *values and show reasonable agreement with the measured data.* © *1997 Elsevier Science Limited.*

1 Introduction

Instrumented microindentation technique has been found an attractive method for measuring hardness and elastic constant of engineering materials. The advantages of this mechanical micro-probe include the ease of performance and the limited sample preparation involved. The technique is particularly favoured for ceramic foils/films and coating materials where sample preparation for other elastic–plastic deformation tests is usually an expensive and time-consuming work.

Considerable research work has been devoted to the development of the instrumented microindentation technique. Both formulae and experimental procedures have been derived, and successfully applied to metallic and ceramic materials.[1–6] However, when they are applied to porous materials, complications due to the very large scatter become obvious.[7–9] Furthermore, if thin porous sheets, e.g. thermal barrier coating layers, are tested, the displacements which are not related to the conventional elastic–plastic deformation of an indentation event contribute to the measured load–depth curve. As a consequence, apparent values for elastic constant and hardness derived from the micro-indentation technique can be significantly lower than these real material values.

In the present study, the indenter displacement as determined from a load–depth curve of an instrumented microindentation test is decomposed into penetration and non-penetration displacements. General equations for evaluating the contributions of the non-penetration displacements to the apparent Young's modulus and hardness are derived. A simplified disk model is proposed to describe the roles of porosity and sample displacements in determining Young's modulus and hardness from the indentation curve. The model is then applied to experimental data obtained from tests completed with both separated and bonded yttria-stabilized zirconia (YSZ) thermal barrier coatings.

2 Hardness and Elastic Constant from Penetration Deformation

Instrumented depth-sensing microindentation testing equipment provides information on the indenter position and indentation load with high precision, e.g. the microindentation machine used in this study, FISCHERSCOPE H100, displays the

*Present address: Department of Mechanical Engineering, James Cook University of Northern Queensland, Townsville, Queensland 4811, Australia.

indenter displacement with accuracy in the nanometer range and load with a resolution of 0·4 mN.[10] Therefore, a fairly accurate load–depth curve can be recorded for a given material. In the case of a flat sample of dense material, the measured indentation curve only depends on the elastic and plastic properties of the material, and indenter geometry. Based on the relationship between the indentation curve and elastic–plastic behaviour, material hardness and elastic parameter can be determined from the measured load–depth curve. The methodology has been described fully in the literature.[1,2]

The principles for determining Young's modulus and hardness from a microindentation test may be iterated with the aid of Fig. 1. Figure 1(a) is a schematic drawing of a typical loading–unloading curve and in Fig. 1(b), the depth parameters of an penetration-induced impression are illustrated. As the ratio C of the projected area A_p to the square of the penetration depth h_p is a constant for a given indenter (e.g. $C = 26{\cdot}43$ for a Vicker's indenter), hardness, which is usually calculated as the applied load, P, divided by the projected area, A_p, can be directly related to h_p by

$$H = P/A_p = P/(C \cdot h_p^2) \tag{1}$$

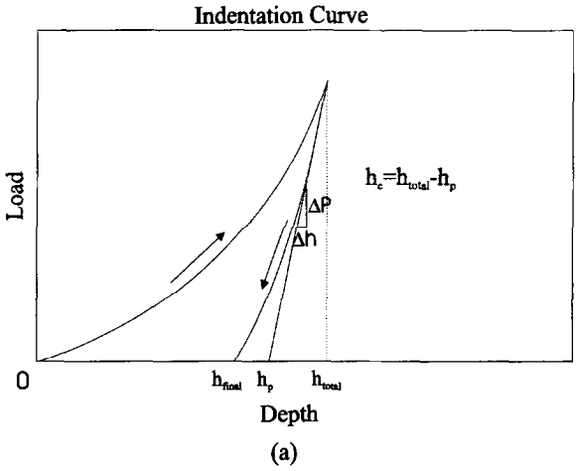

(a)

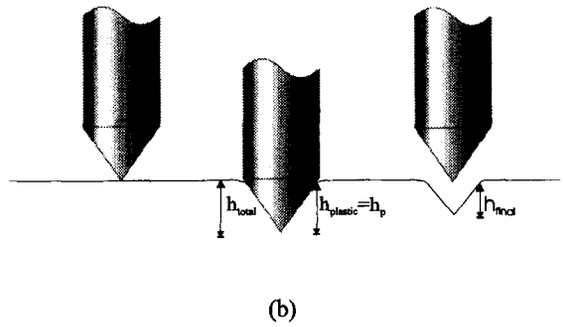

(b)

Fig. 1. Estimation of hardness and elastic constant from an instrumented microindentation test, (a) curve of indentation load versus displacement; (b) definitions of position parameters.

Figure 1 shows that the penetration depth h_p is the equivalent of the plastic depth on the indentation curve and can be obtained by measuring the abscissa intercept of a straight line which starts at the maximum load point and is tangent to the unloading curve.

Young's modulus can be calculated from the unloading slope by adopting Sneddon's flat-ended cylinder punch model.[2,3,11] Based on Sneddon's classical solution of a non-adhesive, rigid, cylindrical flat punch normally loaded on a smooth surface of an elastic solid, the indentation load P is related to the elastic deflection h_e and the radius, a, of the contact area by[1,2]

$$P = \frac{2E}{1 - \nu^2} a \cdot h_e \tag{2}$$

By equating the projected area A_p to the punch area and replacing the elastic constant $E/(1 - \nu^2)$ by the effective elastic constant $E_{eff}/(1 - \nu_{eff}^2)$, one has,[1,4]

$$P = \frac{2E_{eff}}{1 - \nu_{eff}^2} \sqrt{\frac{C}{\pi}} h_p h_e \tag{3}$$

The effective elastic constant $E_{eff}/(1 - \nu_{eff}^2)$ is a parameter which includes the contributions of both the material and the diamond indenter to the indentation curve, and is written as

$$\frac{1 - \nu_{eff}^2}{E_{eff}} = \frac{1 - \nu^2}{E} + \frac{1 - \nu_d^2}{E_d} \tag{4}$$

where subscript d is referred as to the diamond indenter. In the form of unloading slope, eqn (3) may also be written as

$$\frac{dP}{dh} = \frac{2E_{eff}}{1 - \nu_{eff}^2} \sqrt{\frac{C}{\pi}} h_p \tag{3a}$$

3 Influence of Sample Deformation and Porosity

Imperfections in a sample, such as pores and surface irregularities, e.g. valleys and hills, may cause further displacements. Figure 2 outlines some idealized cases where pores and/or an uneven sample surface can produce extra elastic and irrecoverable displacements. A pure elastic displacement may originate from elastic bending of a ligament generated by either a pore or a surface valley left during processing [Fig. 2(a)]. Shown in Fig. 2(b)

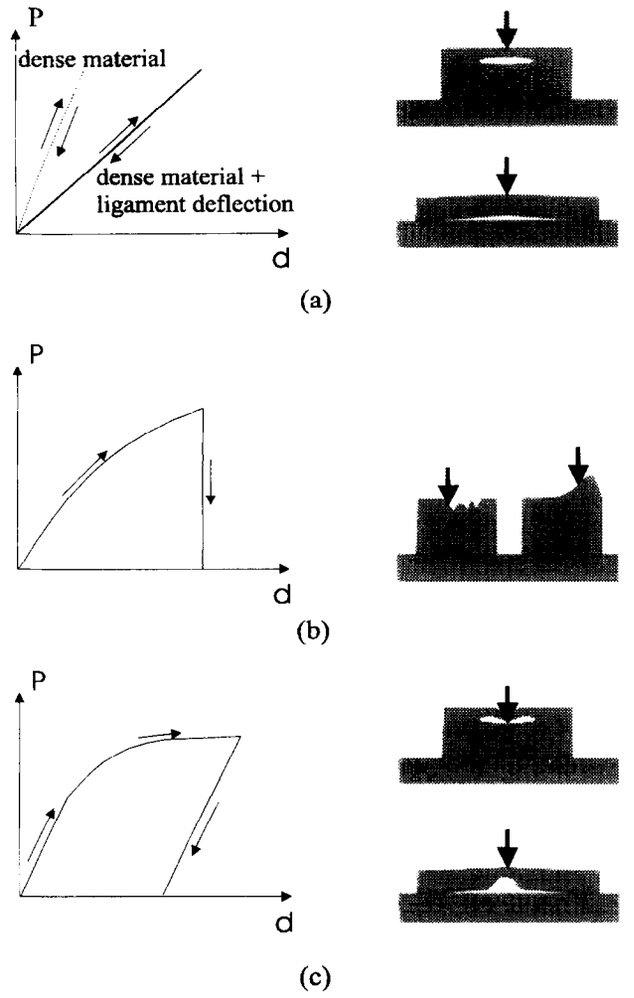

Fig. 2. Extra elastic and/or irrecoverable/plastic displacements due to the pores and sample deformation, (a) elastic, (b) irrecoverable/plastic and (c) elastic–plastic displacements.

are two cases where an irrecoverable displacement can occur because of the slipping of the sample. Figure 2(c) illustrates situations where complete plastic/recoverable displacement occurs after an elastic deformation because of partial ligament fracture. Usually, more than one mechanism of Fig. 2 arises in one test. The extra displacements significantly increase when sample thickness reduces.

The imperfection-induced displacements change the measured elastic constant and hardness through their contributions to the recorded load–depth curve. The influence of these non-penetration displacements on the measured mechanical properties may be analyzed by means of superposition principles. As shown schematically in Fig. 3(a), the imperfection-induced displacement in an instrumented microindentation test can be represented by either a pure elastic or an elastic–plastic load-displacement curve. Without loss of generalization, the imperfection-induced displacement, d, may be expressed as a sum of elastic, P/E_s and plastic/irrecoverable displacement, $d_p(P)$, i.e.

$$d = d_p(P) + P/E_s \tag{5}$$

where E_s is a measure of the stiffness for the elastic deformation of the sample, which is corresponding to the slope of the linear part in Fig. 3(a). After indentation test, the maximum elastic (h_{se}) and plastic/irrecoverable displacement (h_{sp}) due to porosity and surface roughness are $d_p(P_{max})$ and P_{max}/E_s, respectively.

Superposing the elastic/elastic–plastic curve to the penetration curve of the imperfection-free material [curve 1 in Fig. 3(b)], the curve 2 or 3 in Fig. 3(b) may be obtained, which includes the contributions of both material penetration and sample displacement. The total elastic recovery h_{te} estimated from such a 'load-penetration' curve may be written as

$$h_{te} = h_e + h_{se} \tag{6}$$

and the plastic deformation h_{tp},

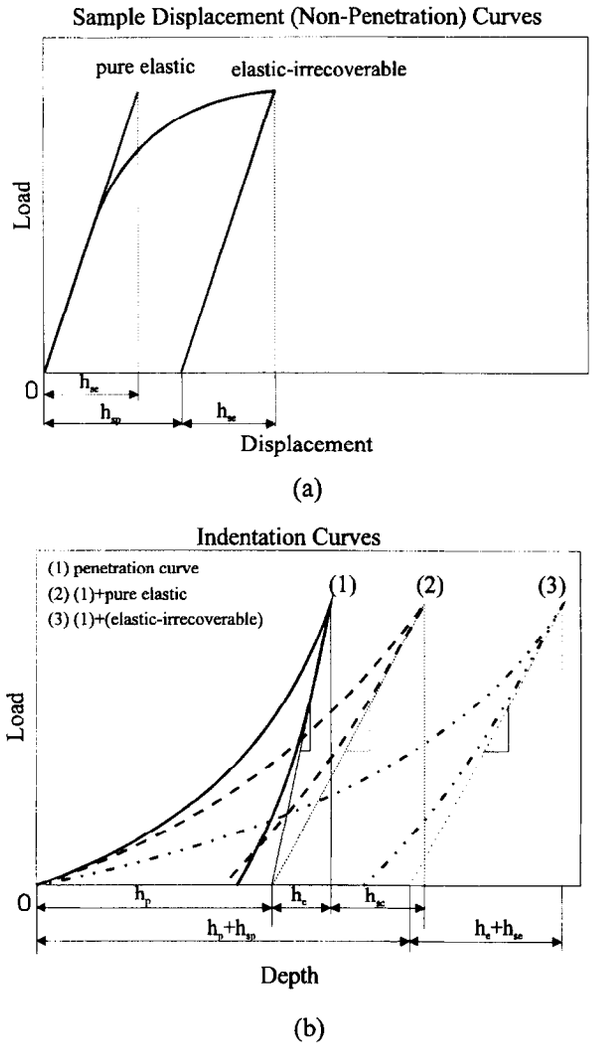

Fig. 3. Influence of non-penetration displacements on the load–depth curve in an instrumented microindentation test: (a) non-penetration load–displacement curves and (b) load–depth curves measured from dense material (1) [same as that in Fig. 1(a)], material with elastic non-penetration deformation (2), and material with elastic–plastic/irrecoverable non-penetration displacements (3).

$$h_{tp} = h_p + h_{sp} \tag{7}$$

As shown in Fig. 3(b), the unloading slopes of the apparent load-penetration curves for the materials including imperfection effects are equal to $P_{max}/(h_e + h_{se})$, which is smaller than P_{max}/h_e, the slope for the imperfection-free material. Also an extra irrecoverable displacement increment, h_{sp}, leads to an increased apparent penetration depth, h_{tp}. As a result, the hardness and elastic constant calculated from such indentation curves are smaller than those for the imperfection-free material.

Considering the fact that in an instrumented indentation test, the apparent elastic and plastic displacements calculated from the load–depth curve include the contributions from both penetration of the indenter itself and sample imperfection related displacements, the depth parameters, h_e and h_p in eqns (1 and 3), should be replaced by h_e and h_{tp} in eqns (6 and 7). Consequently, the apparent hardness H^* is related to the true material hardness H by

$$H^*/H = \frac{1}{[1 + d_p(P_{max})/h_p]^2} \tag{8}$$

and the apparent elastic constant, E^* by

$$\left(\frac{E^*}{1-\nu^2}\right)_{ms} = E/(1-\nu^2)\left\{\left[1 + \frac{E/(1-\nu^2)}{E_d/(1-\nu_d^2)}\right] \times (1 + P_{max}/E_s h_e)(1 + d_p(P_{max})/h_p) - \frac{E/(1-\nu^2)}{E_d/(1-\nu_d^2)}\right\}^{-1} \tag{9}$$

Equations (8 and 9) show that while both the E^* and H^* can be significantly reduced by the imperfection-induced irrecoverable deformation, the imperfection-related elastic deflection only contributes to the elastic constant. The reduction in these two mechanical properties enhances with increasing indentation load. Substituting eqn (8) into eqn (9), the apparent Young's modulus E^* is related to the apparent hardness H^* by

$$\frac{E^*}{E} = \frac{1}{\left[1 + \frac{E/(1-\nu^2)}{E_d/(1-\nu_d^2)}\right]\left(1 + \frac{h_{se}}{h_e}\right)\sqrt{\frac{H}{H^*}} - \frac{E/(1-\nu^2)}{E_d/(1-\nu_d^2)}} \tag{10}$$

The above equation indicates that for a given material and an indenter geometry, the relationship between E^* and H^* essentially depends on the specimen elastic displacement.

4 Applications of Theoretical Model to Experimental Data

Microindentation tests were performed with a plasma-sprayed-yttria stabilized zirconia (YSZ) thermal barrier coating (TBC) system. The TBC samples consisted of a YSZ coating of ~450 μm on a nickel superalloy, IN617 with an ~85 μm interlayer of NiCrAlY. A commercially available instrumented microindentation machine, FISCHERSCOPE H100, was used for the experiments. Both bonded and separated YSZ coating layers were used for the indentation experiments. Indentations were conducted on both cross-sectional and in-plane surfaces of these two types of samples. In the present study, only results from in-plane indentation are discussed in detail. Further experimental details are described elsewhere.[12]

The YSZ/NiCrAlY/IN617 assemblages were polished from the free surfaces towards the interface for indentation testing. After the polishing process, a YSZ layer with thickness of ~310 μm was left on the substrate. The free-standing zirconia layers were obtained by removing mechanically the substrate and bond layers. After removal, the thickness of the separated layers was about 150 μm. Comparing the coating thickness of these two types of samples to that of the as-received TBC samples, an overlap zone of ~10 μm existed. Because the in-plane indentations of these two types of samples were made in the opposite directions, it is expected that in both cases, the same zone in the coatings was examined.

The distributions of apparent hardness and Young's modulus as measured with the instrumented microindentation technique are shown in Fig. 4. A Poisson ratio, $\nu = 0{\cdot}2$, was chosen when calculating the Young's modulus.[13,14] Both H^* and E^* of the YSZ coatings exhibit a large scatter which is more pronounced with respect to hardness values. Nevertheless, the probability plots of both mechanical parameters reveal essentially the same slope. A systematic shift of one order of magnitude between bonded and separated coatings can be observed. For the zirconia coatings bonded on the substrate, the hardness is in a range of 0·1 to 4·3 GPa with an average value of 1·8 GPa and the Young's modulus 8·7 to 54·6 GPa with 30·3 GPa. For the separated coatings, the hardness drops to a range of 0·02 to 1·1 GPa with an average of 0·2 GPa and the elastic modulus 0·6 to 12·5 GPa with 3·2 GPa. Such large differences between the mechanical parameter values of bonded and separated coatings are attributed to the increase in the sample stiffness and the decreasing roughness of sample base surface when a substrate exists. In

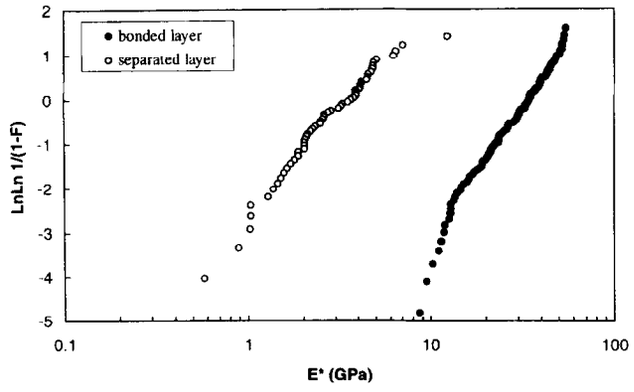

(a)

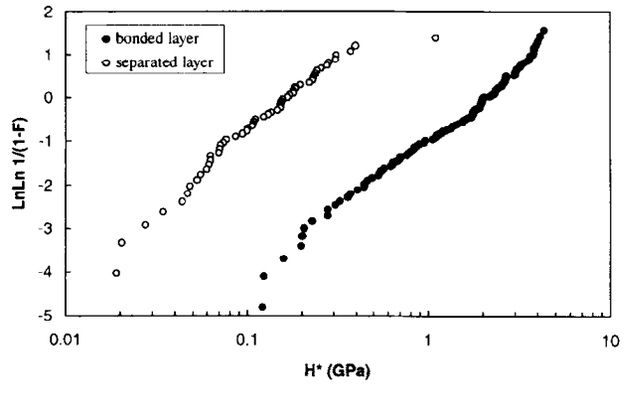

(b)

Fig. 4. Distributions of (a) in-plane Young's modulus and (b) hardness of a YSZ TBC material measured using instrumented microindentation technique.

contrast, the mechanical parameters obtained from the indentations on the cross-section surfaces were in the same range. The measured Young's moduli are 61·3 GPa for the bonded coatings and 58·5 GPa for the separated layers, and the hardness values, 3·7 and 4·1 GPa for these two layers.[12] The difference was only 5% for the Young's modulus and 10% for the hardness. In the cases of cross-section indentation, the specimens were mounted with an epoxy resin base so that the contributions of the sample displacements to the load–depth curve were significantly reduced.

To have a quantitative view of the scattering behaviour and the observed difference, eqns (8 and 9) have been used to explain the results shown in Fig. 4. As the true mechanical properties of the coating material, E and H enter into the relationships, their values have to be determined first. In the present study, it was assumed that the Young's modulus and hardness values could be approximated by the maximum values obtained from the indentation tests.

The maximum hardness measured from the YSZ/NiCrAlY/IN617 assemblages was 4·3 GPa and the plastic displacement corresponding to this hardness value was measured as $h_p = 3$ μm. According to eqn (8), a pore with a depth of $d_p = 14{\cdot}5$ μm, which is typical in the material, reduces the hardness value to the measured lower limit, 126 MPa, and an extra plastic displacement of $d_p = 1{\cdot}7$ μm can yield the average hardness, $H^* = 1{\cdot}8$ GPa. This calculation indicates that the scatter in the hardness values measured with the bonded layers can be induced by the plastic deformation which is related to the typical microstructure size, the pore depths in the material. Comparing the mean hardness of the free-standing layers to that of the YSZ coatings bonded on the substrate, it is found that an average irrecoverable displacement of 10·9 μm, which leads to the shift of the hardness value, was produced by the removal of the bond coat and the substrate. The changes in hardness with increasing irrecoverable displacement are plotted in Fig. 5. Using eqn (9) with $E_d = 1000$ GPa, $v_d = 0{\cdot}25$ for the indenter and $E = 54{\cdot}6$ GPa, $v = 0{\cdot}2$ for the YSZ coating, also E^* is plotted as a function of d_p in Fig. 5. Obviously a small irrecoverable displacement significantly reduces both parameters.

The influence of elastic displacement alone may be modeled by an elastic disk with radius of a, and subjected to a concentrated load P. The disk is either simply supported for sample bending deformation or elastically supported for the pore-related elastic deformation. For an elastically supported circular plate, the elastic displacement at the disk centre can be expressed as

$$w = \alpha w_{max-s} + (1 - \alpha) w_{max-c} \tag{11}$$

where w_{max-s} and w_{max-c} are the elastic displacements at the centres of the disks with simply supported and clamped edges, and α, a constant dependent on the boundary conditions. The solutions of w_{max-s} and w_{max-c} can be found in textbooks (e.g. Timoshenko and Woinowsky-Krieger, 1959),[15]

$$w_{max-s} = \frac{(3 + v)Pa^2}{16\pi(1 + v)D} \tag{12}$$

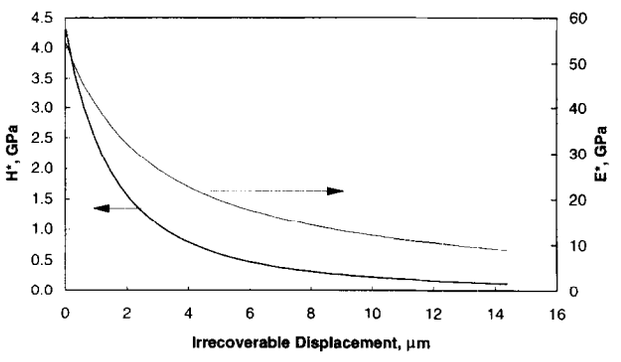

Fig. 5. Influence of irrecoverable/plastic non-indentation displacements on hardness and Young's modulus measured by using instrumented microindentation technique.

and

$$w_{max-c} = \frac{Pa^2}{16\pi D} \tag{13}$$

where D is the flexural rigidity of a plate.

In the present study, the measured maximum Young's modulus was $E^*_{max} = 54{\cdot}6$ GPa and the elastic recovery measured at this point was 1 μm. Considering the influence of elastic deformation related to the pores in the ceramic coatings bonded to the substrate, the model of elastically supported disk with $\alpha = 0{\cdot}5$ was used. Substituting these values and $\nu = 0{\cdot}2$ into eqns (11 to 13), the elastic displacement of a pore-related disk with radius, a, can be obtained as a function of the disk thickness. By setting $d_p(P_{max}) = 0$ in eqn (9), the effects of the pore-induced elastic displacement are calculated and displayed in Fig. 6(a). It can be seen that both increasing disk radius and decreasing ligament thickness reduce significantly the E^* value. Combined elastic and plastic effects are shown in Fig. 6(b) where a pore-related plastic value, $d_p(P_{max}) = 1{\cdot}7$ μm was employed. Figure 6 shows that the Young's modulus can be reduced to the measured lower limit of the bonded layer because of the existence of the pore-related elastic and/or irrecoverable displacements.

The disk model was also applied to the analysis of elastic displacement due to the sample deformation. The disk is simply supported along its edge in this case and includes the pores from the depositing process. Therefore, the average Young's modulus measured from the YSZ/NiCrAlY/IN617 assemblages, $E = 30{\cdot}3$ GPa and $\alpha = 1{\cdot}0$ were used when estimating the elastic stress and strain fields. Considering the dimensions of the real samples and material microstructures, disks with thickness of 80–100 μm and radius of 100–1500 μm were analyzed. Figure 7(a) shows the changes in Young's modulus with both the disk radius and thickness. Obviously, the measured elastic modulus can be significantly decreased by the sample elastic deformation related to the surface valleys and hills. The superposition of elastic and plastic deformation is plotted in Fig. 7(b) which shows the measured Young's modulus for a sample with thickness of 160 μm can be as low as 0·5 GPa. This is in very good agreement with those measured from the free-standing layers.

Finally, plots of elastic modulus as a function of hardness for the YSZ TBC are displayed in Fig. 8. Both Young's modulus and hardness have been normalized with respect to the maximum values. Figure 8 shows that a larger Young's modulus value does not necessarily correlate to a larger hardness. Inspecting eqns (8) and (9), this is not surprising because the apparent Young's modulus

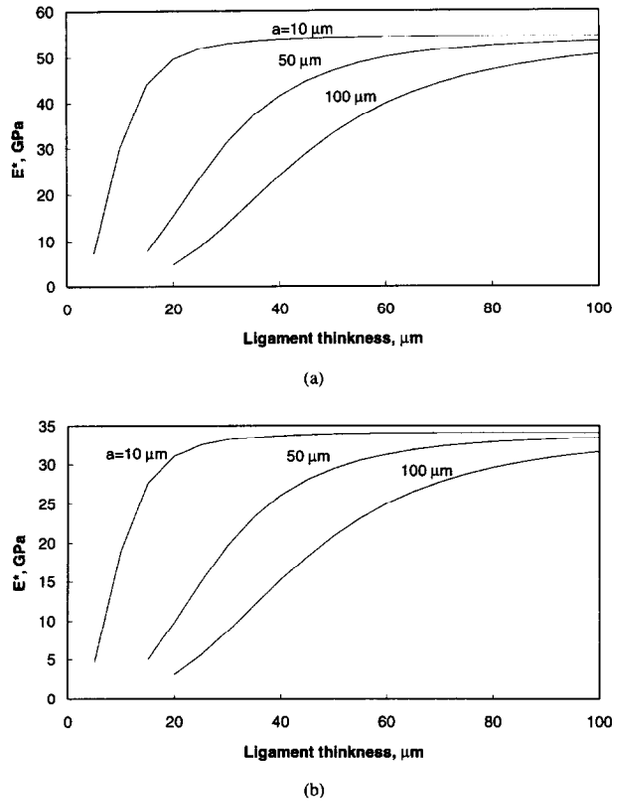

Fig. 6. Contributions of pore-induced non-indentation (a) elastic and (b) elastic–plastic/irrecoverable displacements to the apparent hardness and Young's modulus measured with the bonded YSZ layer.

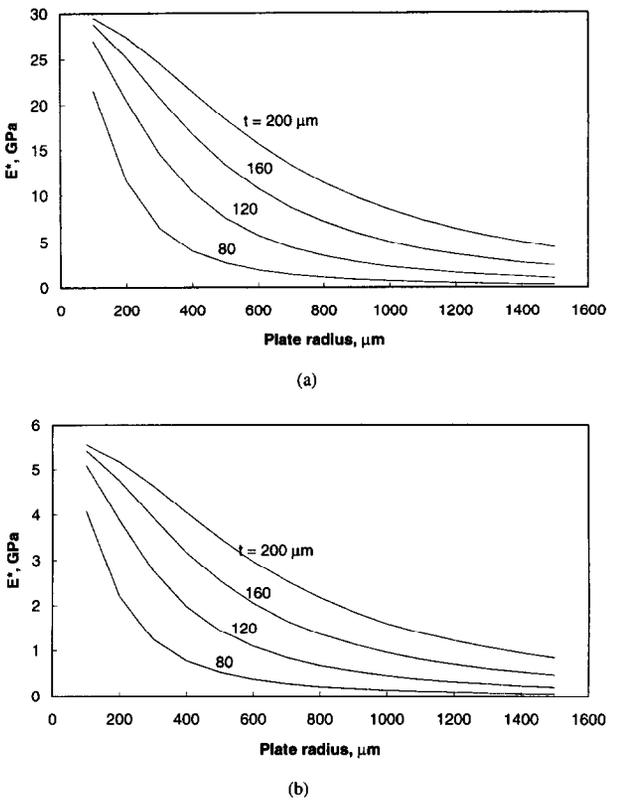

Fig. 7. Contributions of the non-indentation (a) elastic and (b) elastic-irrecoverable/plastic displacements to the apparent hardness and Young's modulus measured with the free-standing YSZ layer.

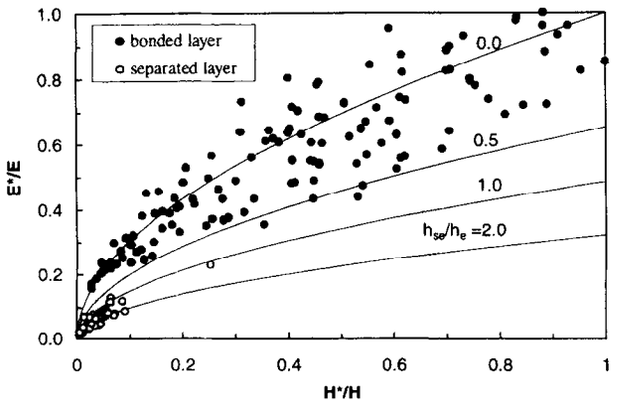

Fig. 8. Comparison of the predicted E^*–H^* curves to the E^*–H^* plots measured with the YSZ TBC materials.

can be changed by the non-penetration elastic deformation even if the hardness is fixed. Similar to the above analysis, the measured maximum mechanical parameter values were used to approximate the real material properties; E^* versus H^* plots for different ratios of sample elastic displacement to penetration elastic recovery may be predicted by using eqn (10). The predicted curves are displayed in Fig. 8 by the solid curves. It can be seen that the predictions with lower h_{se}/h_e ratio are in an agreement with those E–H plots measured from the bonded layer. With the increase in the h_{se}/h_e value, the predicted E–H curves become in line with those from the separated layer. This verifies further that the non-penetration elastic displacements contribute to Young's modulus measured using instrumented microindentation technique, and the contributions become larger when the sample thickness decreases.

5 Conclusions

General equations have been derived for evaluating the influence of non-indentation-induced elastic and irrecoverable/plastic displacements on the apparent hardness, elastic constant and E–H relationship measured with instrumented microindentation technique. An idealised disk model was used to analyze the roles of the non-indentation displacements in controlling the mechanical properties of a thermal barrier coating material. The proposed model was applied to Young's modulus and hardness of the TBC specimen measured with depth-sensing microindentation equipment. It was found that the equations and model could provide a satisfactory explanation for the large scatter in the measured data and the difference between the mechanical properties obtained from the in-plane and cross-section surfaces. Furthermore, the derived E–H relationship was compared to the measured E–H plots The predicted E–H curves were in reasonable agreement with those measured.

Acknowledgements

The authors would like to thank Drs Schubert and Stamm (Siemens–KWU) for stimulating technical discussions about mechanical failure of TBCs. One of the authors (Kai Duan) was financially supported by a KFA-IWE guest scientist program, and is grateful to the TBC program co-ordinator, Dr F. Schubert, for his support and encouragement.

References

1. Doerner, M. F. and Nix, W. D., A method for interpreting the data from depth-sensing indentation instruments. *J. Mater. Res.*, 1986, **1**, 601–609.
2. Loubet, J. L., Georges, J. M. and Meille, G., Vickers indentation curves of elastoplastic materials. In *Microindentation Techniques in Materials Science and Engineering, ASTM STP 889*, ed. P. J. Blau and B. R. Lawn. American Society for Testing and Materials, Philadelphia, 1986, pp. 72–89.
3. Loubet, J. L., Georges, J. M., Marchesini, O. and Meille, G., Vickers indentation curves of magnesium oxide (MgO). *J. Tribology (ASME)*, 1984, **106**, 43–48.
4. Loubet, J. L., Georges, J. M. and Kapsa, Ph., Measurements of thin films adhesion and mechanical properties with indentation curves. In *Mechanics of Coatings*, ed. D. Dowson. Elsevier Applied Science, London, 1989, pp. 429–434.
5. Fougere, G. E., Riester, L., Ferber, M., Weerman, J. R. and Siegel, R. W., Young's modulus of nanocrystalline Fe measured by nanoindentation. *Mater. Sci. Engng.*, 1995, **A204**, 1–6.
6. Tsui, T. Y., Oliver, W. C. and Pharr, G. M., Influence of stress on the measurement of mechanical properties using nanoindentation. Part I: experimental studies in aluminum alloy. *J. Mater. Res.*, 1996, **11**, 752–759.
7. Berndt, C. C., Ratnaraj, R., Karthikeyan, J. and Jun, Y. D., Material property variations in thermally sprayed coatings. In *Thermal Spray Coatings: Properties, Processes and Applications (Proceedings of the Fourth National Spray Conference, 4–10 May 1991, Pittsburgh, Pennsylvania, USA)*, ed. T. F. Bernecki. ASM International, Materials Park, OH, 1992, 199–203.
8. Lin, C.-K., Lin, C.-C. and Berndt, C. C., Simulation of hardness testing on plasma-sprayed coatings. *J. Am. Ceram. Soc.*, 1995, **78**, 1406–1410.
9. Lin, C.-K. and Berndt, C. C., Statistical analysis of microhardness variations in thermal pray coatings. *J. Mater. Sci.*, 1995, **30**, 111–117.
10. Helmut Fischer GmbH+Co, *FISCHERSCOPE H100 Operation Manual*, May 1991.
11. Sneddon, I. N., The relation between load and penetration in the axisymmetric boussinesq problem for a punch of arbitrary profile. *Int. J. Engng. Sci.*, 1965, **3**, 47–57.
12. Duan, K. and Steinbrech, R. W., Mechanical properties of thermal barrier coatings by microindentation. Submitted, 1996.
13. Steffens, H.-D. and Fischer U., Correlation between microstructure and physical properties of plasma sprayed zirconia coatings. In *Thermal Spray Technology New Ideas and Processes (Proceedings of the National Thermal Spray Conference, 24–27 October 1988, Cincinnati, Ohio, USA)*, ed. D. L. Houck. ASM International, Metals Park, OH., 1989, pp. 167–173.
14. Rybicki, E. F., Shadley, J. R., Xiong, Y. and Greving, D. J., A cantilever beam method for evaluating Young's modulus and Poisson's ratio of thermal barrier coatings. *J. Thermal Spray Tech.*, 1995, **4**, 377–383.
15. Timoshenko, S. and Woinowsky-Krieger, S., *Theory of Plates and Shells*, McGraw-Hill Book Company, New York, 1959.